Available online at www.sciencedirect.com
SCIENCE DIRECT®
International Journal of Hydrogen Energy 30 (2005) 327–339
International Journal of HYDROGEN ENERGY
www.elsevier.com/locate/ijhydene

A numerical study of H_2–air partially premixed flames

Alejandro M. Briones, Suresh K. Aggarwal*

Department of Mechanical and Industrial Engineering, University of Illinois at Chicago, P.O. Box 4348, M/C 251, 2039 Engineering Research Facility, Chicago, IL 60607, USA

Received 16 March 2004; received in revised form 29 March 2004; accepted 6 April 2004

Abstract

A numerical investigation of the structure of hydrogen/air partially premixed flames (PPFs) in a counterflow configuration is reported. The partially premixed flame structure is characterized by two spatially distinct reaction zones. Unlike hydrocarbon/air PPFs, the fuel is partially consumed in the rich premixed zone, where H, O, and OH are the major intermediate species, with the remaining fuel being consumed in the nonpremixed zone. In both the reaction zones, consumption of reactants occur primarily through reactions $H+O_2 \leftrightarrow OH+O$ (R1), $H_2+O \leftrightarrow OH+H$ (R2), $H_2+OH \leftrightarrow H_2O+H$ (R3), and $H+O_2+M \leftrightarrow HO_2+M$ (R9). Maximum heat release occurs in the rich premixed zone through reactions R9 and R3. Interactions between the two reaction zones involve the transport of heat from the nonpremixed to the premixed reaction zone and the transport of H_2 from the premixed to the nonpremixed zone. The flame response to variations in equivalence ratio (ϕ) and strain rate (a_s) is characterized. Increasing ϕ and/or a_s causes the two reaction zones move closer, and eventually merge with each other. Further increase in ϕ leads to a nonpremixed flame, while that in a_s leads to stretch-induced extinction. Finally, differences between the structures of hydrogen PPFs and hydrocarbon-fuel PPFs are highlighted.

Keywords: Hydrogen partially premixed; Equivalence ratio; Global strain rate

1. Introduction

Partially premixed flames (PPFs) contain multiple (e.g. two or more) reaction zones, and their structure is determined by the interactions between these reaction zones. PPFs occur widely in practical combustion systems either by design or under conditions arising due to various phenomena, such as poor mixing, spray vaporization [1], flame lift-off [2], and local extinction followed by reignition in turbulent flames [3]. For instance, the combustion processes in diesel [1] and spark-ignition [4] engines are dominated by two-stage or partially premixed combustion.

In this paper, we report a numerical study of hydrogen-air PPFs established in a counterflow configuration. Our study is motivated by several considerations. First, the detailed structure of hydrogen PPFs has not been investigated in previous studies, which have mostly focused on hydrocarbon PPFs using methane [5–15] or *n*-heptane fuels [16–18]. Our literature review indicates only two previous investigations on hydrogen PPFs, one dealing with the effects of diluents on NO_x emission in a counterflow PPF [19], and the other concerning the propagation characteristics of a triple flame in a H_2/air mixing layer [20,21].

Second, the structure of H_2/air PPFs may be significantly different from that of hydrocarbon fuel/air PPFs, and this warrants a fundamental investigation of H_2/air PPFs. For instance, in hydrocarbon PPFs, most of the fuel is consumed in the rich premixed zone to produce intermediate fuel species such as H_2, CO, and C_2H_2, which are transported to and consumed in the nonpremixed reaction zone. Thus, the premixed reaction zone chemistry is characterized by the partial oxidation of hydrocarbon fuel to produce intermediate fuel species (e.g. H_2, CO, and C_2H_2), while the nonpremixed zone chemistry is characterized by the oxidation of these species to produce H_2O and CO_2. In contrast, in H_2/air PPFs, the fuel is only partially consumed in the rich premixed zone,

* Corresponding author. Tel.: 1-312-996-2235; fax: 1-312-413-0447.
E-mail address: ska@uic.edu (S.K. Aggarwal).

0360-3199/$ 30.00 © 2004 International Association for Hydrogen Energy. Published by Elsevier Ltd. All rights reserved.
doi:10.1016/j.ijhydene.2004.04.007

with the remaining fuel being consumed in the nonpremixed zone. Consequently, the fuel oxidation chemistry in the two reaction zones and the interactions between them are significantly different in the hydrogen and hydrocarbon-fuel PPFs. Another fundamental difference may be due to the transport and chemistry of radical species in these flames [9].

Third, a fundamental investigation of hydrogen/air PPFs allows us to study the flame response to stretch and diffusional-thermal instability over a wider range of Lewis numbers. The counterflow PPFs are positively stretched, and the local Lewis number in the rich premixed zone is less than or near unity for hydrocarbon/air PPFs, while it is greater than unity for hydrogen/air PPFs. Consequently, the hydrogen/air PPFs can be used to characterize flame response to diffusional-thermal instability over a wider range of Lewis numbers. Moreover, due to the high diffusivity and reactivity of hydrogen–air mixtures, the hydrogen/air PPFs are expected to have a significantly wider partially premixed combustion regime in terms of strain rate and equivalence ratio.

Finally, there is growing world-wide interest to move towards a hydrogen-based economy due to many potential advantages of hydrogen fuel over conventional fossil fuels. Apart from being environmentally clean, hydrogen represents potentially an unlimited source of energy since it can be readily formed from water through electrolysis, as well as from fossil fuels through partial oxidation and reforming. In addition, it has higher energy per unit mass (about 2.6 times that of gasoline), superior ignition characteristics, and significantly wider flammability limits compared to hydrocarbon fuels. However, due to its high flammability and low volumetric energy density, many important issues pertaining to hydrogen safety and storage are still being addressed. Numerous efforts are currently underway focusing on the use of hydrogen in various propulsion and energy applications, including fuel cells and hydrogen-based IC engines [22–24]. In this context, blending hydrogen with hydrocarbon fuels also represents a promising approach to increase the use of hydrogen, and improve the emission and performance of various combustion systems [25–27]. Studies reported by Al-Baghdadi [25], Choudhuri and Gollahalli [26], Kumar et al. [27], and Naha and Aggarwal [28] have shown that using blends of hydrogen and hydrocarbon fuels can improve both the emission and combustor performance.

2. Objective

The major objective of the present study is to examine the detailed structure of a counterflow H_2/air PPF, and to characterize differences between the structures of hydrogen and hydrocarbon-fuel PPFs. As discussed above, the study is motivated by the considerations that previous investigations have mostly focused on hydrocarbon-fuel PPFs, and there are significant differences between the structures of hydrocarbon-fuel and hydrogen PPFs. A counterflow configuration is employed so that the investigation can focus on characterizing (1) the detailed flame structure and interactions between the reaction zones, (2) the dominant reaction pathways in each reaction zone, (3) flame response to changes in equivalence ratio (ϕ) and strain rate a_s, and (4) the differences between the hydrogen and hydrocarbon-fuel PPFs.

3. Physical–numerical model

The physical model considers a PPF in a counterflow configuration. The flame is established by igniting the fuel–air mixture formed by two opposing jets, one containing a rich H_2–air mixture and the other containing air. The flame structure can be controlled by independently specifying the fuel stream equivalence ratio (ϕ) and the global strain rate (a_s). The global strain rate is approximated using the formula [6]:

$$a_s = (2|v_o|/L) \cdot (1 + |v_f|\sqrt{\rho_f}/|v_o|\sqrt{\rho_o}). \quad (1)$$

In the above equation, L is the separation distance between the two jets, v_o the oxidizer jet velocity, v_f the fuel jet velocity, and ρ_f and ρ_o the mixture densities in the fuel and oxidizer jets, respectively. The distance between the two nozzles is 1.27 cm. The velocities of the fuel and oxidizer streams are obtained by using Eq. (1) and matching the momenta of the two streams. The temperatures of the fuel and oxidizer nozzles are set at 300 K. The radiative heat loss is not considered since its effect is known to be insignificant for moderately to highly stretched flames simulated in the present study.

Simulations of H_2–air PPFs established at a given ϕ and a_s are performed using the OPPDIF [29] code in the CHEMKIN package [30]. The grid independence of the results was established by controlling the GRAD and CURV parameters, both of which were set at 0.1, and using adaptive regridding to resolve the structures of both the premixed and nonpremixed reaction zones. This required the number of grid points to be 290 for the base case.

It is important to note that due to the high diffusivity and reactivity, H_2–air mixtures have significantly higher flame speeds and wider flammability limits. Consequently, the ranges of ϕ and a_s characterizing the partially premixed combustion regime for H_2–air flames may be significantly different compared to those for hydrocarbon fuel–air flames. Consequently, extensive simulations were performed to identify the ranges of ϕ and a_s for which the H_2–air PPFs exhibit a double-flame structure. These simulations yielded the following double-flame regime, $3.0 < \phi < 6.0$ and $500 < a_s < 2400$, for H_2–air PPFs.

4. Results and discussion

4.1. Validation

The reaction mechanism used for our simulation is due to Mueller et al. [31]. The mechanism is listed in Table 1, and

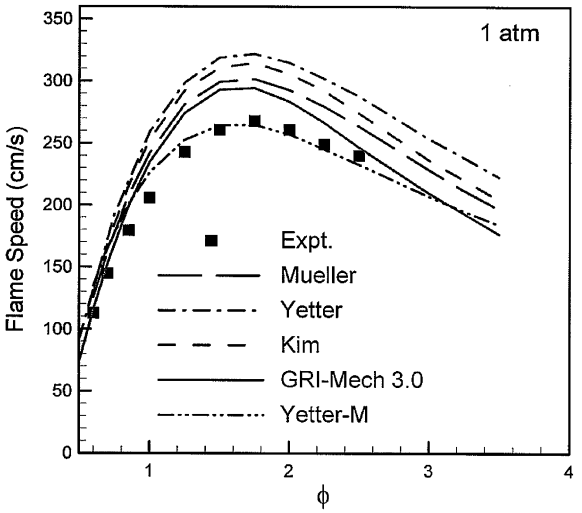

Fig. 1. Comparison of measured [32] and predicted unstretched laminar flame speeds for H_2/O_2/He flames as a function of equivalence ratio at 1 atm with $O_2/(O_2+He) = 0.125$. Predictions are based on the Mueller et al. [31], Yetter et al. [37], Kim et al. [38], GRI-Mech 3.0 [39], and modified Yetter and Shepherd [40] mechanisms.

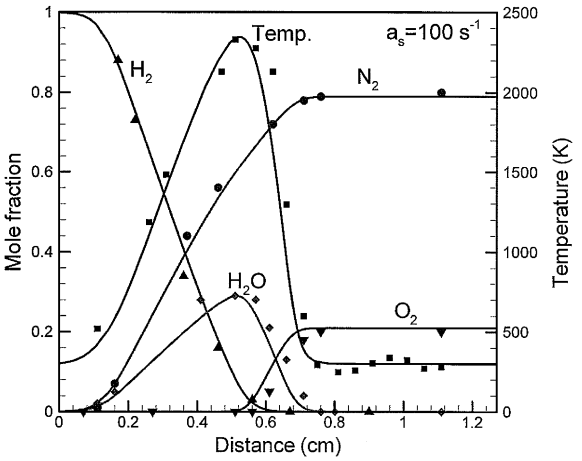

Fig. 2. Comparison of measured [42] and predicted temperature and species mole fraction profiles for an H_2/air diffusion flame at $a_s = 100\ s^{-1}$ and 1 atm. Predictions are based on the Mueller et al. [31] mechanism.

includes 19 reversible reactions and eight non-inert species. The mechanism has been previously validated using experimental data for perfectly stirred reactor [31], freely propagating flames [32–34], and nonpremixed flames [35]. Since the present study deals with the simulations of H_2/air PPFs, we provide additional validations using experimental data for premixed, nonpremixed, and partially premixed flames.

For the first validation, the PREMIX [36] and CHEMKIN [30] packages were used to compute the freely propagating flame speed of H_2/O_2/He mixture as a function of ϕ at 1 atm. Fig. 1 presents a comparison between the flame speed measured by Tse et al. [32], and the flame speeds computed using the Mueller et al. [31], Yetter et al. [37], Kim et al. [38], GRI-Mech 3.0 [39], and modified Yetter and Shepherd [40] mechanisms. While all the mechanisms are able to qualitatively reproduce the experimental flame speeds, they exhibit significant quantitative differences, especially for the fuel rich conditions. The modified Yetter mechanism yields the best agreement with the experimental data, while the Yetter mechanism shows the maximum difference. In a separate study, we compared the computed flame speeds, based on these five mechanisms, with measurements of Tse et al. [32] and Aung et al. [33] over a wide range of pressures. The Mueller mechanism was found to be the most accurate for reproducing the effect of pressure on the flame speed as well as the well-known reaction limits for H_2–air mixtures [41]. Consequently, this mechanism was selected for further validation.

For the second validation, we compared the structure of a H_2–air nonpremixed flame, computed using the Mueller et al. [31] mechanism, with the measurements of Brown et al. [42]. The computations were performed using the OPPDIF [29] and CHEMKIN [30] packages. Fig. 2 presents a comparison of the measured and predicted flame structures in terms of the temperature and major species profiles. These profiles show good agreement between the predictions and measurements, providing further validation of the Mueller et al. [31] mechanism.

For another validation, we computed the structure of an H_2/air PPF using the Mueller et al. [31] mechanism, and compared the predictions with the measurements of Rortveit et al. [19]. As shown in Fig. 3, a reasonably good agreement is indicated between the predicted and measured temperature profiles. As discussed in the cited study, the temperature along the centerline was measured using a B-type thermocouple with Pt–6%Rh versus Pt–30%Rh with a coating to prevent catalytic reactions on the thermocouple, and there were relatively large uncertainties in the thermocouple data, which may be due to the high burning velocities of hydrogen.

4.2. Partially premixed flame structure

Fig. 4 presents the structure of an H_2–air PPF established at $\phi = 3.0$ and $a_s = 600\ s^{-1}$. The flame structure is depicted in terms of the temperature, axial velocity, and species mole fraction profiles. As mentioned earlier, the range of double-flame regime for hydrogen PPFs is approximately given by $3.0 < \phi < 6.0$ and $500 < a_s < 2400$. Thus, the hydrogen PPFs are established at relatively high strain rates and over wider levels of premixedness compared to the hydrocarbon-fuel PPFs. This difference is due to the higher laminar flame speeds and wider flammability limits of

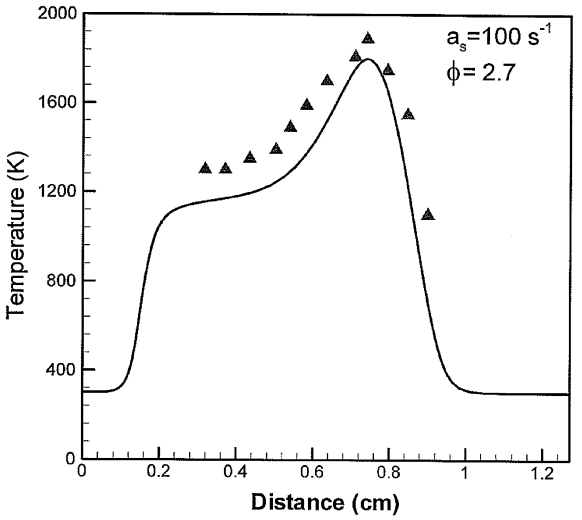

Fig. 3. Comparison of measured [19] and predicted temperature profiles for a 30%H_2/5.5%O_2/64.5%N2 PPF at $a_s = 100\ s^{-1}$ and 1 atm. Predictions are based on the Mueller et al. [31] mechanism.

H_2–air mixtures compared to those of hydrocarbon fuel–air mixtures. For the flame depicted in Fig. 4, the fuel and air stream velocities were specified as 266.9 and 190.5 cm/s, respectively. The fuel stream velocity was chosen such that it is above the laminar flame speed ($\sim$ 220 cm/s) at $\phi = 3.0$.

The flame in Fig. 4 exhibits a double flame structure containing two reaction zones, a rich premixed reaction zone on the fuel side and a nonpremixed reaction zone on the oxidizer side. Previous investigators have employed various criteria, such as maximum heat release rate [43], maximum temperature gradient [17], and local maxima in certain species profiles [6] to identify the location of the rich premixed zone. In the present study, the upstream location of this zone is defined by the local minimum in axial velocity, and its downstream location by a local minimum in H_2 mole fraction. Based on this definition, the rich premixed zone thickness is about 0.11 cm, and it contains 79 grid points. The peak temperature in the rich premixed zone is about 1500 K, which is lower than that of the corresponding unstretched premixed flame at $\phi = 3.0$. This may be attributed to the fact that the flame is positively stretched, and the local Lewis number in the premixed zone is about 2.0 [43]. This is in accord with the results of Wu and Law [44], who reported that the adiabatic temperature of a premixed flame with Lewis number above (below) unity is reduced (increased) when a flame is positively stretched.

The location of the nonpremixed reaction zone is defined by the maximum temperature [17]. As indicated in Fig. 4(a), the nonpremixed zone is located just downstream of the stagnation plane. Based on the heat release rate profile shown in Fig. 4(c), the nonpremixed reaction zone thickness is about 0.16 cm, and it contains 39 grid points.

The axial velocity profile (cf. Fig. 4 (a)) indicates that the axial velocity decreases to a local minimum, which represents the stretched laminar flame speed just ahead of the rich premixed zone, and then increases in the premixed zone due to thermal expansion. In general, laminar flame speeds have been calculated by linearly extrapolating the stretched flame speed to zero stretch using counterflow twin flames [43,44], and inwardly and outwardly propagating spherical flames [33,34,43,45]. The present results suggest that one can also employ a counterflow PPF to compute the flame speeds, since the local stretch rate is simply defined as the negative of the maximum local axial velocity gradient ahead of the rich premixed zone. This aspect is discussed further in a later section.

The premixed zone is characterized by the partial consumption of H_2, production of H radicals and H_2O, and complete consumption of O_2. The partial consumption of fuel in the rich premixed flame represents another important difference between H_2/air and hydrocarbon fuel/air PPFs. Previous investigations of methane [9,11] and *n*-heptane [17,18] PPFs have shown that the fuel is completely consumed in the premixed zone to provide intermediate fuel species such as CO and H_2 (and C_2H_2 in some cases), which are then transported to and consumed in the nonpremixed reaction zone. In contrast, for hydrogen PPFs, the fuel is only partially consumed in the premixed zone, with the remaining fuel being transported to and consumed in the nonpremixed zone. Another difference between the H_2/air and hydrocarbon fuel/air PPFs pertains to the chemical activity in the region between the two reaction zones. For hydrocarbon fuel/air PPFs, previous studies [9,17] have shown that this region has negligible chemical activity. However, for hydrogen/air PPFs, there is chemical activity in this region, characterized by the production of H_2 through the recombination of H radicals. This is clearly indicated by the increasing H_2 mole fraction and decreasing H mole fractions in this region (cf. Fig. 4a).

The nonpremixed zone, which is located just downstream of the stagnation plane, is characterized by the consumption of the remaining hydrogen, and the peak values of the temperature and H_2O mole fraction. The peak temperature is about 2150 K, which is lower than the adiabatic flame temperature of $\sim$ 2350 K. This is due to the significantly broadened reaction zone compared to that of a nonpremixed flame, and heat transfer to the rich premixed zone. In both the reaction zones, the local temperature peak coincides with the corresponding peaks in H_2O and H mole fractions, and where the consumption of O_2 occurs. This indicates that the heat release is associated with H_2O formation, which is further illustrated in Fig. 4c. In addition, a rate of production analysis [41] indicated that R9 and R3 are the dominant exothermic reactions, while R3 is the dominant reaction that produces H_2O. The maximum heat release occurs in the rich premixed zone.

Fig. 5 presents the relative contributions of various reactions to the production/consumption of H_2, O_2, H_2O, O, H, and OH species. Note that the contributions to the production

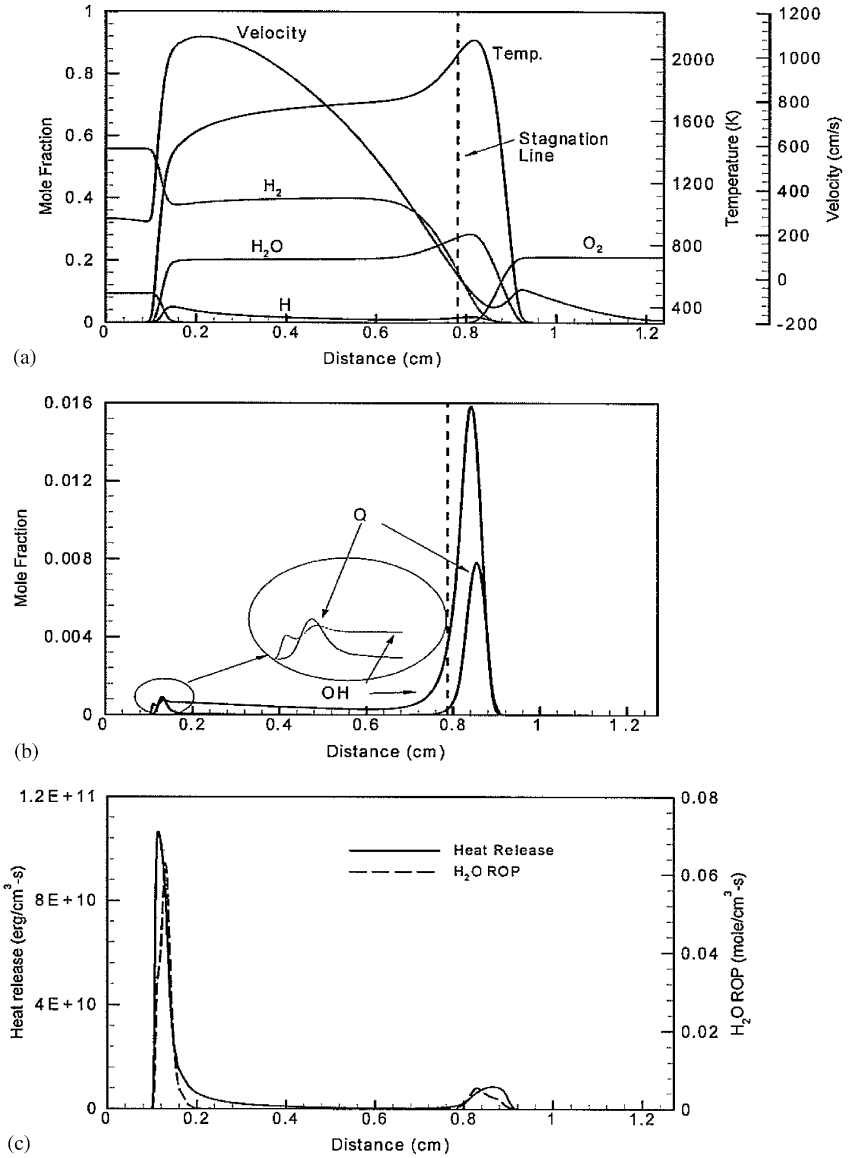

Fig. 4. Profiles of temperature, axial velocity, species mole fractions, heat release rate, and H_2O rate of production (ROP) plotted versus distance from the fuel nozzle for a H_2–air PPF established at $\phi = 3.0$ and $a_s = 600\ s^{-1}$. Species H_2, O_2, H_2O, and H are plotted in Fig. 4(a), while species OH and O in Fig. 4(b). The stagnation plane is indicated by the dashed line.

and consumption of each species are considered separately, but over the entire axial domain including both reaction zones. The ratio of total production to consumption rate of each species is also indicated in each figure. For example, as indicated in Fig. 5(a), reactions R3 and R5 contribute about 75% and 80% to the total consumption and production of H_2, respectively. However, the total production to consumption rate of H_2 is 0.14 indicating that the production of H_2 is only about one seventh of consumption. It is also worth noting that the ratio of total production to consumption rate of radical species is close to unity. Nevertheless, the plots are useful to identify the dominant reactions associated with the net production/consumption of H, O, and OH radicals.

4.3. Interactions between the two reaction zones

In order to investigate interactions between the two reaction zones, we examine the dominant reactions in each reaction zone, and the heat and mass transport between them. Fig. 6 presents the reaction rate profiles of the important

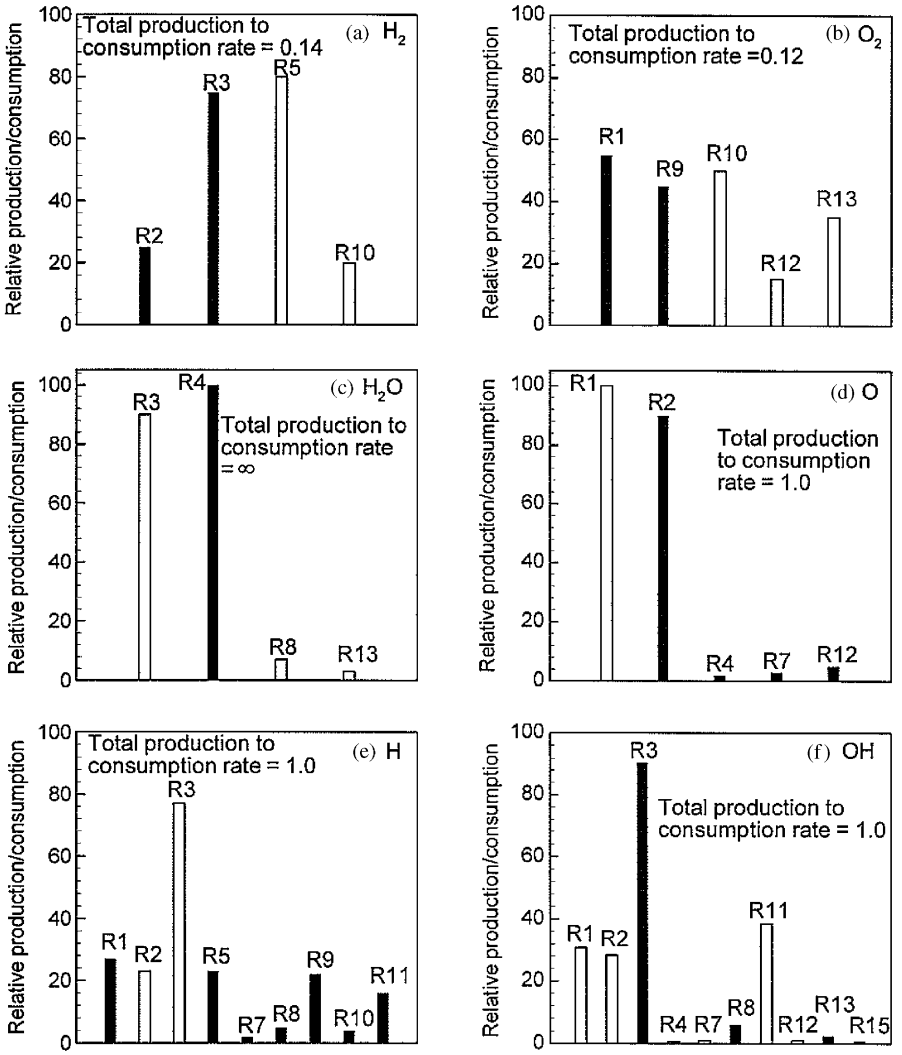

Fig. 5. Relative production/consumption of species H_2, O_2, H_2O, O, H, and OH, obtained using a rate of production analysis, for the PPF discussed in the context of Fig. 4. Open bars indicate production, while close bars indicate consumption.

reactions associated with the production/consumption of H_2 and O_2 in the rich premixed zone. The molecular hydrogen is consumed through reactions R3 and R2, and produced through reactions R5 and R10. The reaction rate profiles of O_2 (cf. Fig. 6(b)) indicate that the oxygen is consumed through reactions R1 and R9, and produced through reactions R10 and R13. The other three reactions, R6, R12, and R14, involved in the O_2 production/consumption were found to be negligible and are not shown in the figure. Another important observation from Fig. 6 is that the chain branching reactions R1, R2, and R3 peak almost at the same axial location, which also coincides with the location of the maximum heat release. However, the peak of reaction R9 is located upstream of that of reaction R1, and this is related to the well-known explosion or reaction limits of H_2–O_2 mixtures. As discussed by Christiansen et al. [41], in the first reaction limit, reactions R1 and R9 occur in the high- and low-temperature regions of the flame, respectively, preventing these reactions from competing with each other. Our results presented in Fig. 6 are consistent with this observation.

Fig. 7 presents the reaction rate profiles of the dominant reactions associated with the production/consumption of H_2 and O_2 in the nonpremixed zone. R2 and R3 are the dominant reactions consuming H_2 in the nonpremixed zone. This is in accord with the results reported by Azzoni et al. [11] dealing with the simulation of methane–air PPFs. In the cited study, R2 and R3 were found to be dominant reactions consuming H_2 in nonpremixed zone. The dominant O_2 production/consumption reactions in the nonpremixed zone are presented in Fig. 7(b). Similar to the premixed reaction

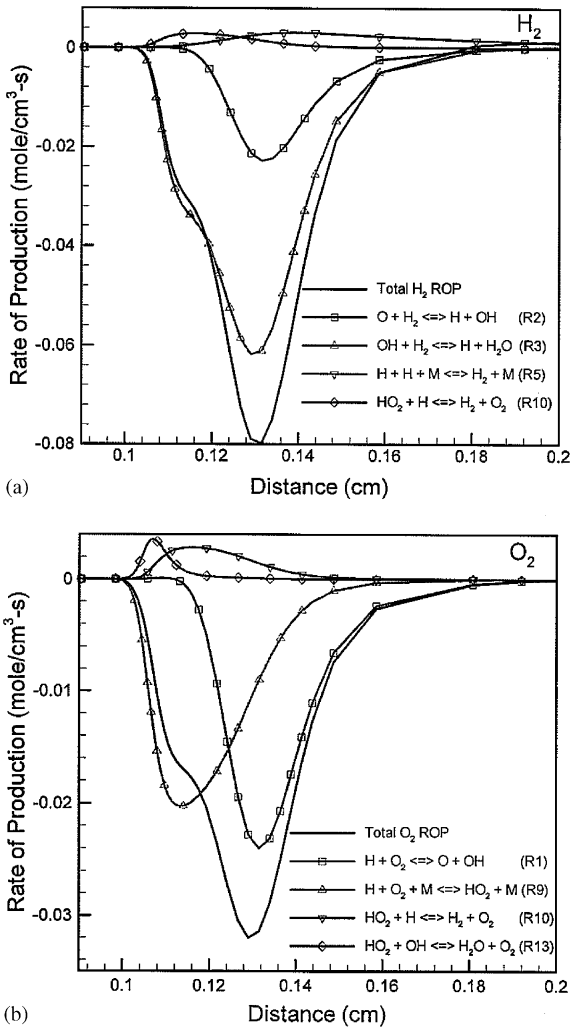

Fig. 6. Reaction rate profiles of dominant reactions associated with the production/consumption of H_2 (6a) and O_2 (6b) in the rich premixed reaction zone of the H_2–air PPF shown in Fig. 4. The total production/consumption rates are also shown.

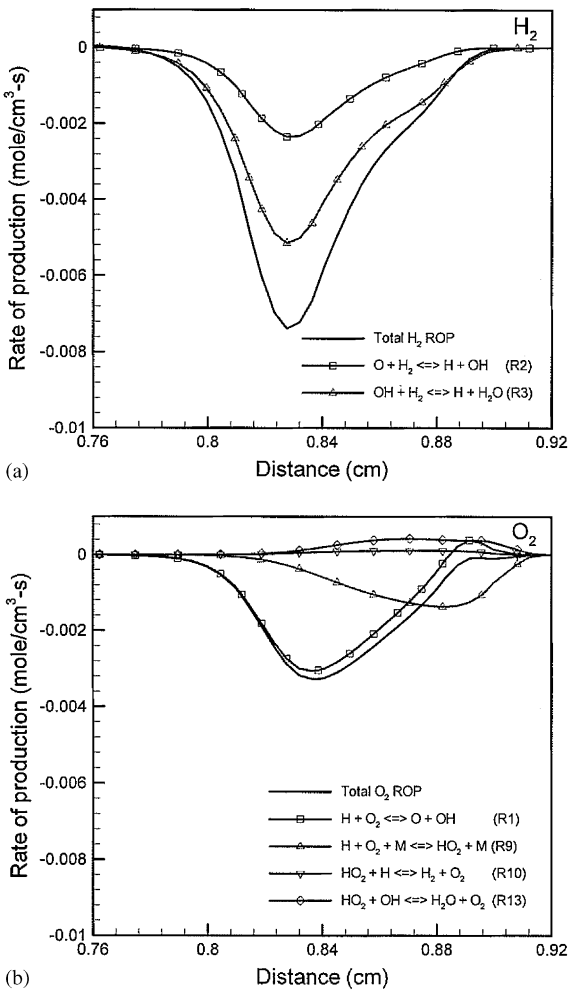

Fig. 7. Reaction rate profiles of dominant reactions associated with the production/consumption H_2 (Fig. 7a) and O_2 (Fig. 7b) in the nonpremixed reaction zone of the H_2–air PPF shown in Fig. 4. The total production/consumption rates are also shown.

zone, R1 and R9 are the dominant reactions consuming O_2 in the nonpremixed zone, indicating that the consumption of O_2 occurs mostly through its reactions with H radicals. In addition, the R9 peak occurs downstream (e.g., in the low-temperature region or closer to the oxidizer nozzle) of that of reaction R1, which is again related to the behavior of reactions R1 and R9 in the first reaction limit. In summary, the dominant reactions associated with the production/consumption of H_2 and O_2 exhibit similar behavior in the two reaction zones. This represents another important difference between the hydrogen and hydrocarbon-fuel PPFs. In the latter flame, the premixed zone is characterized by the fuel pyrolysis/consumption chemistry, while the nonpremixed zone is characterized by the CO and H_2 oxidation chemistry.

In order to further analyze the interactions between the two reaction zones, we examine the species transport in the flow field. Fig. 8 presents the profiles of mass fraction and mass flux of H_2 and O_2 species. The mass flux includes both the convective and diffusive fluxes, and is given by $\dot{m}_i'' = \dot{m}'' \cdot Y_i - \rho \cdot D_{i-j} \cdot \mathrm{d}Y_i/\mathrm{d}x$. The mass fraction and mass flux of H_2 decrease sharply in the premixed zone due to its partial consumption to produce H_2O. However, in the region between the two reaction zones, both the mass fraction and mass flux of H_2 increase slowly, indicating the production of H_2 in this region. As discussed earlier in the context of Fig. 5, the production of H_2 in this region occurs mainly through the recombination of hydrogen radicals (R5). Another important observation from Fig. 8(a) is that the mass flux of H_2 is positive in the entire domain, implying that

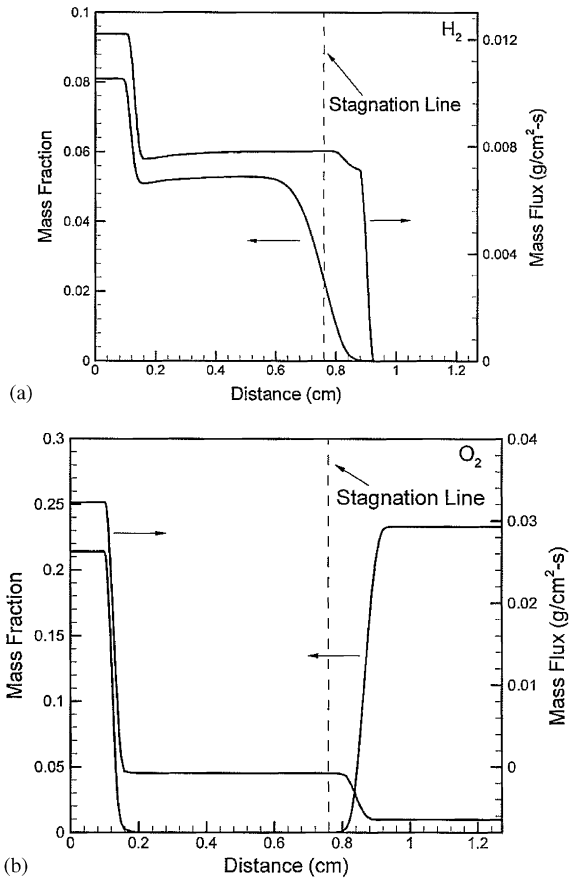

Fig. 8. Mass fraction and mass flux profiles of H_2 (8a) and O_2 (8b) for the PPF discussed in the context of Fig. 4.

H_2 is transported from the rich premixed zone to the nonpremixed zone. Moreover, the general shape of H_2 mass flux profile is similar to that of the mass fraction profile indicating that the mass flux is generally dominated by convection. However, near the stagnation plane, the diffusion becomes important, since H_2 mass fraction starts decreasing for $x > 0.6$ cm, while its mass flux does not. Beyond the stagnation plane, the H_2 mass flux again decreases sharply due to its consumption in the nonpremixed zone. Here, the H_2 mass flux is entirely due to diffusion because its direction is towards the oxidizer nozzle while the convection is towards the stagnation plane, i.e., the diffusive flux delivers H_2 to the nonpremixed zone. In summary, the convection of H_2 is dominant from the fuel nozzle to the axial location of about 0.6 cm, and then the diffusion of H_2 becomes dominant from this location until it gets oxidized the nonpremixed zone.

The oxygen mass flux profile in Fig. 8(b) indicates that O_2 is transported primarily by convection from each nozzle to the rich premixed and nonpremixed reaction zones, respectively, where it is fully consumed. Consequently, its

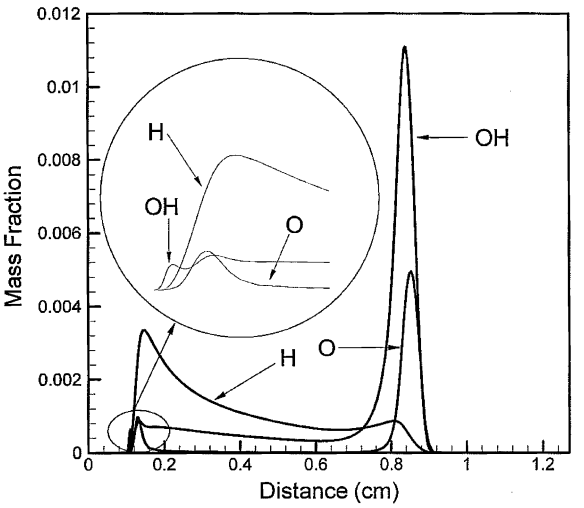

Fig. 9. Mass fraction profiles of H, O, and OH radicals for the PPF discussed in the context of Fig. 4.

mass flux is zero in the region between the two reaction zones. As expected, the mass flux profiles of H_2 and O_2 indicate a typical premixed combustion behavior in the premixed zone, and a nonpremixed combustion behavior in the nonpremixed zone. In the premixed zone, the transport of both H_2 and O_2 is in the same direction and toward the reaction zone, while in the nonpremixed zone, their transport is in the opposite direction, but toward the reaction zone.

Fig. 9 presents the mass fraction profiles of H, O, and OH radicals. As expected, these radical species exhibit their peak values in the two reaction zones. However, the peak H mass fraction is higher than those of O and OH in the rich premixed zone, while those of O and OH are higher in the nonpremixed zone. This is due to the higher concentrations of H_2 and O_2 in the rich premixed and nonpremixed zones, respectively. The decrease in H mass fraction in the region between the two reaction zones is due to the conversion of H radicals to H_2 through the recombination reaction (R5), as mentioned earlier. The OH mass fraction profile exhibits two peaks in the rich premixed zone, and this can be explained by examining its mass flux profile, as discussed below.

Fig. 10 presents the mass flux profiles of H, O, and OH radicals. The species mass flux profiles can be used to gain further insight not only about the transport behavior of a given species, but also about the net production/consumption rate of that species, since the gradient of the mass flux represents the net production or consumption rate. Production of major radical species (i.e., H, O, and OH) in the rich premixed zone occurs at $x \approx 0.13$ cm. This is indicated by the positive slope of H, O, and OH mass flux profiles in the premixed zone. Here, the atomic hydrogen is produced through reactions R2 and R3, while O is produced through R1, and OH through the combined effects of R1, R2, and R3. The contribution of each of these reactions is indicated

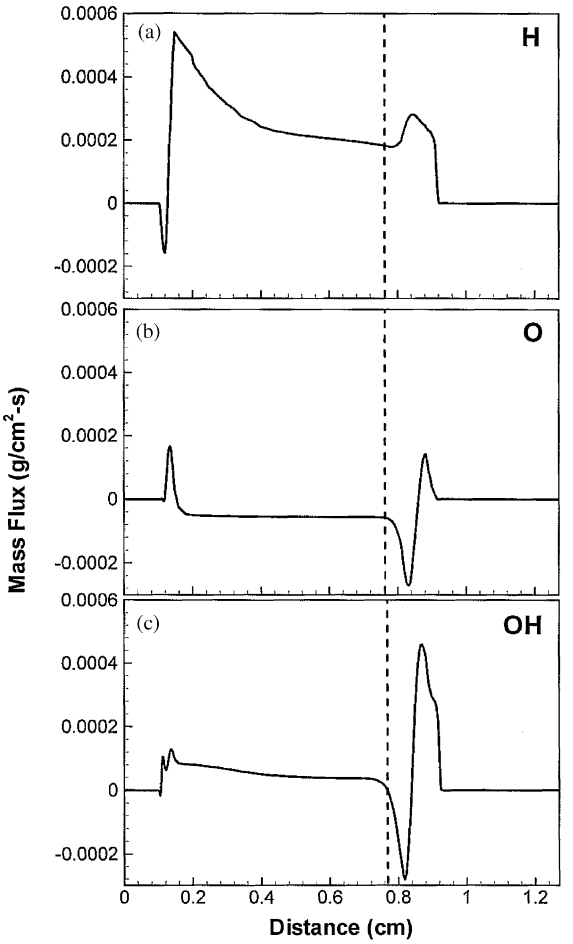

Fig. 10. Mass flux profiles of H, O, and OH radicals for the flame discussed in the context of Fig. 4. The dashed lines represent the location of the stagnation plane.

more clearly in Fig. 5. The H radicals produced in this zone are transported in both the upstream and downstream directions.[1] The H radicals transported upstream react with O_2 to produce HO_2 through R9, and HO_2 then produces OH through R11 (cf. Figs. 5 and 6). The production of OH is indicated by the first peak in the OH mass flux profile in Fig. 10c. The H radicals transported downstream are partially consumed in the premixed zone through reaction R1 to produce O and OH radicals. The production of O is indicated by the peak in the O mass flux profile, while that of OH by the second peak in the OH mass flux profile. The remaining H radicals are transported downstream from the premixed zone and are consumed through the recombination reaction R5 to produce H_2, which is consistent with the earlier observation regarding the production of H_2 through the recombination of hydrogen radicals in the region between the two reaction zones. In addition, downstream of the premixed zone, O radicals are consumed through reaction R2, and OH through the combined effects R3, R1, and R2.

The mass flux profiles in the nonpremixed zone indicate that there is production of H radicals and consumption of O and OH radicals in the upstream region of the nonpremixed zone ($x \approx 0.82$ cm). Molecular hydrogen transported from the premixed zone reacts with O and OH to produce H radicals through reactions R2 and R3 (cf. Figs. 5 and 7). Within the nonpremixed zone, O radicals are produced through reaction R1, while OH radicals are produced through R1 and R2. These radicals are then transported from this zone in both the upstream (due to diffusion) and downstream (due to convection) direction. It is also important to note that transport of H radicals in this zone is predominantly due to diffusion, since the convection transport is in the upstream direction, i.e., toward the stagnation plane. Further downstream in the nonpremixed zone ($x = 0.88$ cm), the H radicals react with the incoming O_2 to produce HO_2 through R9 which is then consumed through R11 and R12 (cf. Fig. 5) to produce OH, which in turn is consumed through R4 to produce O radicals. This appears to be in contradiction with Fig. 5, which shows that the production/consumption of OH through R4 is negligible. However, R4 produces OH in the upstream part of the nonpremixed zone and consumes OH in the downstream part of this zone. It is also interesting to note that there is a leakage of O radicals from the nonpremixed to the premixed zone. This is indicated by the negative value of the O species mass flux.

There are two other important observations from Fig. 10. First, the H radical activity is more pronounced compared to those of O and OH radicals in the rich premixed zone, while O and OH radicals are more active in the nonpremixed zone. This is due to the higher concentration of H_2 in the rich premixed zone and of O_2 in the nonpremixed zone. Second, for hydrogen PPFs, the interactions between the two reaction zones involve the transport of H_2 from the rich premixed to the nonpremixed zone, and of heat from the nonpremixed to the rich premixed zone. In contrast, for hydrocarbon-fuel PPFs, such interactions involve the transport of "intermediate fuel" species (i.e., H_2, CO, and C_2H_2) from the rich premixed to the nonpremixed zone, and that of heat and H radicals from the nonpremixed to the rich premixed zone.

4.4. Effects of ϕ and a_s on the flame structure

The response of a PPF to variations in premixedness (ϕ) and aerodynamic strain (a_s) provides fundamental information about the flame response to stretch and diffusive-thermal instability, as well as its propagation and extinction characteristics. In addition, it provides information about the merging behavior of the reaction zones, and the partially premixed combustion regime. While these aspects have been

[1] For the premixed zone, upstream refers towards the fuel nozzle, while downstream refers towards the stagnation plane. For the nonpremixed zone, upstream refers towards the stagnation plane, while downstream refers towards the air nozzle.

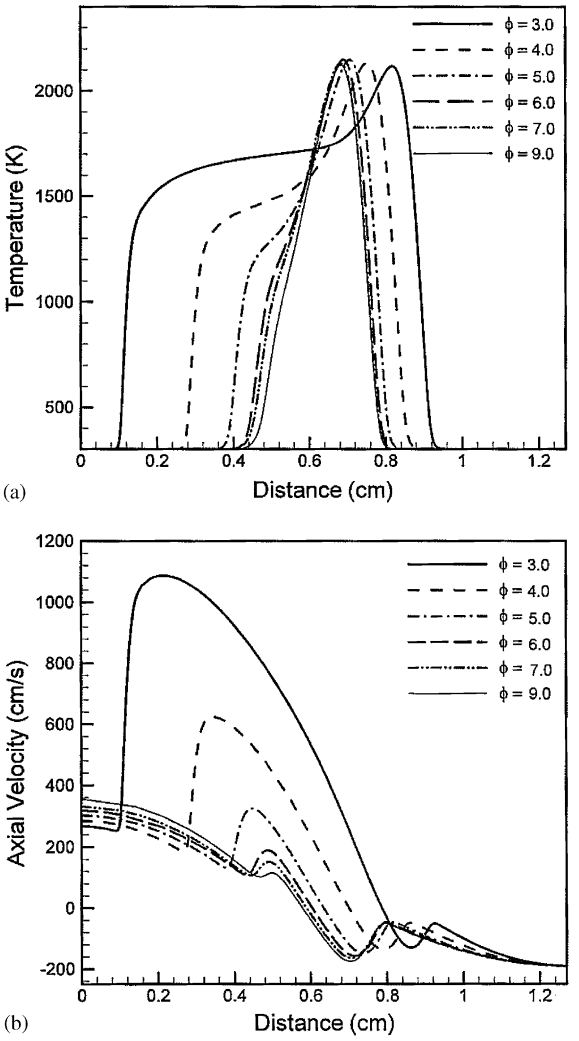

Fig. 11. Temperature (11a) and velocity (11b) profiles for H_2/air PPFs established at a global strain rate of $a_s = 600\ s^{-1}$, and $\phi = 3.0$, 4.0, 5.0, 6.0, 7.0 and 9.0.

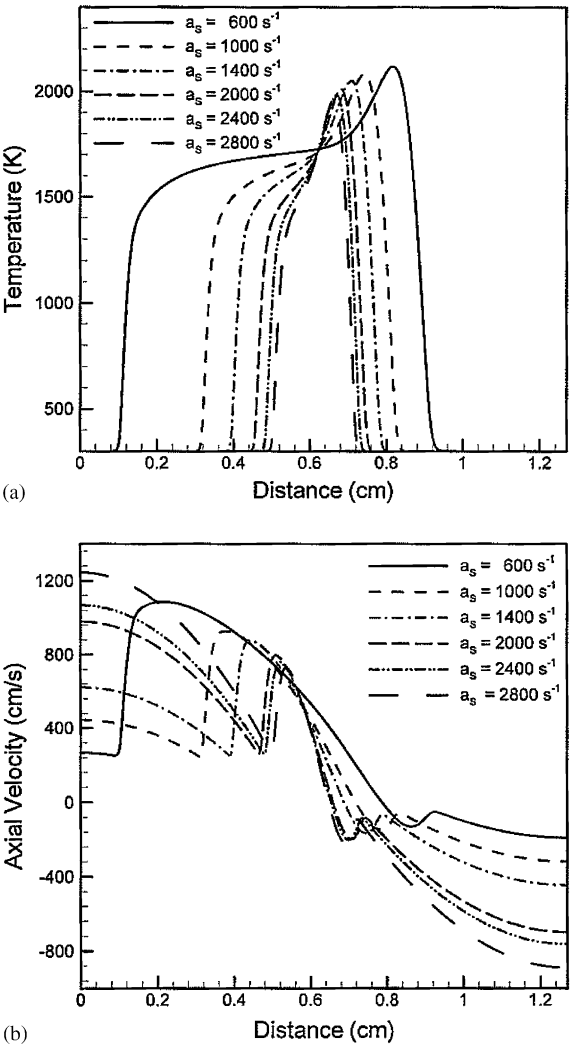

Fig. 12. Temperature (12a) and axial velocity (12b) profiles for H_2/air PPFs established at $\phi = 3.0$, and global strain rates of 600, 1000, 1400, 2000, 2400, and 2800 s^{-1}.

extensively investigated for hydrocarbon-fuel PPFs, those for hydrogen PPFs have not been reported.

Fig. 11 presents the temperature and velocity profiles for H_2–air PPFs established at different equivalence ratios, and at a global strain rate of $a_s = 600\ s^{-1}$. As ϕ is increased, it reduces the spatial separation between the two reaction zones, and thereby enhances interactions between them. The two reaction zones appear to merge for $\phi \geqslant 6.0$, indicating a merged-flame regime for higher ϕ. Another important observation from Fig. 11 is that a change in ϕ mostly affects the rich premixed reaction zone. As ϕ is increased, the premixed zone moves closer to the nonpremixed zone, and its peak temperature decreases. In contrast, the maximum temperature in the nonpremixed zone remains essentially the same as ϕ is increased from 3.0 to 9.0. The location of the premixed zone for a given ϕ is related to the variation of flame speed (s_u) with ϕ. As ϕ is increased, the flame speed decreases, and, consequently the premixed reaction zone moves downstream and is stabilized at a location where the local flow velocity matches with the flame speed. This is clearly depicted by the axial velocity profiles in Fig. 12(b). Thus, as ϕ is increased, the merging of the two reaction zones results from a decrease in flame speed, which causes the rich premixed zone to move closer to the nonpremixed zone.

In order to characterize the response of PPFs to flame stretch and Lewis number, Fig. 12 presents the temperature and axial velocity profiles for H_2–air PPFs established at different strain rates, and at an equivalence ratio of $\phi = 3.0$. For these flames, the Lewis number upstream of the rich

premixed zone is about 2.0 [43], while that for hydrocarbon fuel–air PPFs is less than unity. In addition, H_2–air PPFs are established at much higher strain rates compared to the hydrocarbon fuel–air PPFs. As a_s is increased, the flow velocity increases, and consequently, the rich premixed zone moves downstream to a location where the stretched flame speed matches the local flow velocity. This is clearly indicated by both the temperature and axial velocity profiles presented in Fig. 12. In addition, the maximum temperature, which is located in the nonpremixed zone, decreases due to a decrease in the residence time caused by the increasing strain rate. This also lowers the temperature in the rich premixed zone due to interactions between the two reaction zones. For $a_s > 2400\ s^{-1}$, the two reaction zones are nearly merged, indicating a merged-flame regime at such high strain rates.

Previous researchers have employed various configurations, such as counterflow twin flames [43,44], and inwardly and outwardly propagating spherical flames [33,34,43,45], to determine the flame response to stretch and to extract the unstretched flame speed. Here, we employ the counterflow partially premixed flame configuration to extract such information. In this configuration, the stretched flame speed can be determined from the axial velocity profiles presented in Fig. 12(b). The axial velocity decreases to a local minimum upstream of the rich premixed zone, and then increases sharply to the maximum value in this zone. As discussed in Ref. [43], the local minimum axial velocity upstream of the premixed zone defines the stretched flame speed (s_u), while the maximum velocity in the premixed zone defines the stretched flame speed (s_b) relative to the burnt mixture. The unstretched laminar flame speed relative to the burnt mixture (s_b^0) is then obtained by plotting s_b versus the flame stretch, which is defined as the negative of the maximum axial velocity gradient ahead of the premixed zone, and linearly extrapolating to zero stretch. Subsequently the laminar unstretched flame speed (s_u^0) is obtained using the equation:

$$s_u^0 = (\rho_b \cdot s_b^0)/\rho_u. \quad (2)$$

For $\phi = 3.0$, this yields the unstretched flame speed as $s_u^0 = 207$ cm/s, which is consistent with the value (219 cm/s) reported by Tse et al. [32]. Thus, PPFs can be employed to obtain unstretched flame speeds in a manner similar to that used by Sun et al. [43] to compute flame speeds from counterflow twin flames.

5. Conclusions

We have investigated the detailed structure of H_2–air partially premixed flames established at atmospheric pressure in a counterflow configuration. Based on an extensive validation of the various hydrogen oxidation mechanisms, the Mueller mechanism has been used in the present study. The simulations using this mechanism show good agreement with the available experimental data for premixed, nonpremixed and partially premixed flames. Important observations are:

1. Similar to hydrocarbon-fuel PPFs, the hydrogen PPF structure is characterized by two spatially distinct reaction zones, namely a rich premixed zone on the fuel side and a nonpremixed zone on the air side. However, unlike hydrocarbon-fuel PPFs, the fuel is partially consumed in the rich premixed zone, where H, O, and OH are the major intermediate species, with the remaining fuel transported to and consumed in the nonpremixed zone. Another difference between the hydrogen and hydrocarbon-fuel PPFs is that for the former, the nonpremixed zone is characterized by the H_2 oxidation chemistry, while for the latter it is characterized by the H_2 and CO oxidation chemistry. In addition, for the former, there is production of H_2 through the recombination of hydrogen radicals in the region between the two reaction zones, while there is negligible chemical activity in this region for the latter.
2. Other differences between the hydrogen and hydrocarbon-fuel PPFs are due to different Lewis numbers, partially premixed regimes, and interactions between the two reaction zones. The Lewis number upstream of the rich premixed zone is greater than unity for hydrogen flames, while it is less than unity for hydrocarbon flames. The partially premixed regime is significantly wider for hydrogen flames compared to that for hydrocarbon flames. In addition, for hydrogen flames, interactions between the two reaction zones involve the transport of H_2 from the rich premixed to the nonpremixed zone and that of energy from the nonpremixed to the rich premixed zone. In contrast for hydrocarbon flames, interactions involve the transport of intermediate fuel species (CO, H_2, and C_2H_2) from the rich premixed to the nonpremixed zone, and that of energy and radical species (H and OH) from the nonpremixed to the rich premixed zone.
3. For hydrogen PPFs, the fuel oxidation chemistry is similar in the two reaction zones. It involves the consumption of H_2 primarily through reactions R2 and R3, and that of O_2 through reactions R1 and R9. However, the rich premixed zone has higher concentration of H radicals, while the nonpremixed zone has higher concentrations of O and OH radicals. The maximum heat release occurs in the rich premixed zone mostly through reactions R9 and R3.
4. As ϕ and/or a_s are increased, the two reaction zones move closer to each other and merge at a critical value of these two parameters. Further increase in ϕ at a fixed a_s leads to a nonpremixed flame structure, while that in a_s leads to flame extinction. However, the variation in ϕ mostly affects the rich premixed zone, whereas that in a_s primarily affects the nonpremixed reaction zone. The merging of the two reaction zones is related to the effect of ϕ and/or a_s on the flame speed associated with the rich premixed reaction zone.

5. A counterflow PPF represents another possible configuration for the computation of laminar flame speeds. PPFs are positively stretched flames, and the local minimum in the axial velocity profile upstream of the rich premixed zone defines the stretched flame speed (s_u), while the maximum velocity in the premixed zone defines the stretched flame speed (s_b) relative to the burnt mixture. The unstretched laminar flame speed can be obtained by systematically subtracting out the effect of strain.

Acknowledgements

This research was supported by the NSF Combustions and Plasma Systems Program for which Dr. Farley Fisher has been the Program Director. We thank Professor S.D. Tse for providing us the hydrogen–air reaction mechanisms as well as the premixed flame speed data. Many stimulating discussions with Professor I.K. Puri are gratefully appreciated.

Appendix A. Kinetic modeling of the H_2/O_2 reaction

The H_2/O_2 reaction mechanism is shown below (Table 1).

References

[1] Flynn FF, Durrett RP, Hunter GL, zur Loye AO, Akinyemi OC, Dec JE, Westbrook CK. Diesel combustion: an integrated view combining laser diagnostics, chemical kinetics and empirical validation. SAE, Paper 99-01-0509, 1999.

Table 1
H_2/O_2 reaction mechanism. Units are cm^3-mol-s-kcal-K; $k = AT^n \exp(-E_a/RT)$

	ΔH^0_{298}	A	n	E_a
H_2/O_2 *chain reactions*				
R1. $H + O_2 = O + OH$	16.7	1.91×10^{14}	0.00	16.44
R2. $O + H_2 = H + OH$	1.85	5.08×10^{4}	2.67	6.29
R3. $H_2 + OH = H_2O + H$	−15.01	2.16×10^{8}	1.51	3.43
R4. $O + H_2O = OH + OH$	16.88	2.97×10^{6}	2.02	13.4
H_2/O_2 *dissociation/recombination reactions*				
R5. $H_2 + M = H + H + M$[a]	104.2	4.58×10^{19}	−1.40	104.38
$H_2 + Ar = H + H + Ar$	104.2	5.84×10^{18}	−1.10	104.38
R6. $O + O + M = O_2 + M$[a]	−119.1	6.16×10^{15}	−0.50	0.00
$O + O + Ar = O_2 + Ar$	−119.1	1.89×10^{13}	0.00	−1.79
R7. $O + H + M = OH + M$[a]	−102.3	4.71×10^{18}	−1.0	0.00
R8. $H + OH + M = H_2O + M$[a]	−119.2	2.21×10^{22}	−2.00	0.00
$H + OH + At = OH + Ar$	−119.2	8.41×10^{21}	−2.00	0.00
Formation and consumption of HO_2				
R9. $H + O_2 + M = HO_2 + M$[a]	−49.1	k_0 3.5×10^{16}	−0.41	−1.12
$H + O_2 + Ar = HO_2 + Ar$	−49.1	k_0 1.5×10^{15}	0.00	−1.00
$H + O_2 = HO_2$[c]		k_∞ 1.48×10^{12}	0.60	0.00
R10. $HO_2 + H = H_2 + O_2$	55.1	1.66×10^{12}	0.00	0.82
R11. $HO_2 + H = OH + OH$	−36.47	7.08×10^{13}	0.00	0.30
R12. $HO_2 + O = OH + O_2$	−52.23	3.25×10^{13}	0.00	0.00
R13. $HO_2 + OH = H_2O + O_2$	−70.11	2.89×10^{13}	0.00	−0.50
Formation and consumption of H_2O_2				
R14. $HO_2 + HO_2 = H_2O_2 + O_2$[b]	−38.53	4.20×10^{14}	0.00	11.98
$HO_2 + HO_2 = H_2O_2 + O_2$[b]		1.30×10^{11}	0.00	−1.63
R15. $H_2O_2 + M = OH + OH + M$	−51.14	k_0 1.20×10^{17}	0.00	45.5
$H_2O_2 + Ar = OH + OH + Ar$	−51.14	k_0 1.90×10^{16}	0.00	43.0
$H_2O_2 = OH + OH$[c]		k_∞ 2.95×10^{14}	0.00	48.4
R16. $H_2O_2 + H = H_2O + OH$	−68.05	2.41×10^{13}	0.00	3.97
R17. $H_2O_2 + H = H_2 + HO_2$	−16.57	4.82×10^{13}	0.00	7.95
R18. $H_2O_2 + O = OH + HO_2$	−14.70	9.55×10^{6}	2.00	3.97
R19. $H_2O_2 + OH = H_2O + HO_2$[b]	−31.58	1.00×10^{12}	0.00	0.00
$H_2O_2 + OH = H_2O + HO_2$[b]		5.8×10^{14}	0.00	9.56

[a]Efficiency factors for the collision partners of this pressure dependent reaction are: $\varepsilon(H_2O)$=12.0; $\varepsilon(H_2) = 2.5$; and $\varepsilon(Ar) = 0.75$. All other species have efficiencies equal to unity. When a rate constant is declared specifically for an argon collision partner, the efficiency of argon is set to zero when determining M for the same reaction.

[b]Reactions 14 and 19 are expressed as the sum of the two rate expressions.

[c]Reaction 9 is given as a true fit with $F_c(N_2) = 0.5$ and $F_c(Ar) = 0.45$. Reaction R15 is given as a true fit with $F_c = 0.5$.

[2] Lee BJ, Chung SH. Combust Flame 1997;109(1–2):266–81.
[3] Vervisch L. Proc Combust Inst 2000;28:11–24.
[4] Haworth DC, Blint RJ, Cuenot B, Poinsot TJ. Combust Flame 2000;121(3):395–417.
[5] Barlow RS, Karpetis AN, Frank JH, Chen J-Y. Combust Flame 2001;127(3):2102–18.
[6] Tanoff MA, Smooke MD, Osborne RJ, Brown TM, Pitz RW. Proc Combust Inst 1996;26:1121–8.
[7] Bennett BAV, Mcenally CS, Pfefferle LD, Smooke MD. Combust Flame 2000;123(4):522–46.
[8] Zhu XL, Gore JP, Karpetis AN, Barlow RS. Combust Flame 2002;129(3):342–5.
[9] Xue HS, Aggarwal SK. AIAA J 2001;39(4):637–45.
[10] Xue HS, Aggarwal SK, Osborne RJ, Brown TM. AIAA J 2002;40(6):1236–8.
[11] Azzoni R, Ratti S, Aggarwal SK, Puri IK. Combust Flame 1999;119(1–2):23–40.
[12] Shu Z, Choi CW, Aggarwal SK, Katta VR, Puri IK. Combust Flame 1999;111(4):296–311.
[13] Shu Z, Choi CW, Aggarwal SK, Katta VR, Puri IK. Combust Flame 1999;118(1–2):91–107.
[14] Choi WC, Puri IK. Combust Flame 2000;123(1–2):119–39.
[15] Law CK, Zhu DL, Li TX, Chung SH, Kim JS. Combust Sci Technol 1989;64(4–6):199–232.
[16] Li SC, Williams FA. Proc Combust Inst 2000;28:1031–8.
[17] Xue HS, Aggarwal SK. AIAA J 2002;40(11):2289–97.
[18] Xue HS, Aggarwal SK. Combust Flame 2003;132(4):723–41.
[19] Rortveit GJ, Hustad JE, Li S-C, Williams FA. Combust Flame 2002;130(1–2):48–61.
[20] Im HG, Chen JH. Combust Flame 1999;119(4):436–54.
[21] Im HG, Chen JH. Combust Flame 2001;126(1–2):1384–92.
[22] Heffel JW. Int J Hydrogen Energy 2003;28(8):901–8.
[23] Kabat DM, Heffel JW. Int J Hydrogen Energy 2002;27(10):1093–102.
[24] Heffel JW. Int J Hydrogen Energy 2003;28(11):1285–92.
[25] Al-Baghdadi MAS. Renewable Energy 2003;28(9):1471–8.
[26] Choudhuri AR, Gollahalli SR. Int J Hydrogen Energy 2000;25(5):451–62.
[27] Kumar MS, Ramesh A, Nagalingam B. Int J Hydrogen Energy 2003;28(10):1143–54.
[28] Naha S, Aggarwal SK. Combust Flame 2003, submitted for publication.
[29] Lutz AE, Kee RJ, Grcar JF, Rupley FM. Report No. SAND96-8243, Sandia National Laboratories, 1996.
[30] Kee RJ, Rupley FM, Meeks E, Miller JA. Report No. SAND96-8216, Sandia National Laboratories, 1996.
[31] Mueller MA, Kim TJ, Yetter RA, Dryer FL. Int J Chem Kinetics 1998;31(2):113–25.
[32] Tse SD, Zhu DL, Law CK. Proc Combust Inst 2000;28: 1793–800.
[33] Aung KT, Hassan MI, Faeth GM. Combust Flame 1997; 112(1–2):1–15.
[34] Kwon OC, Faeth GM. Combust Flame 2001;124(4):590–610.
[35] Fotache CG, Sung CJ, Sun CJ, Law CK. Combust Flame 1998;112(3):457–71.
[36] Kee RJ, Grcar JF, Smooke MD, Miller JA, Meeks E. Report No. SAND85-8240, 1985.
[37] Yetter RA, Dryer FL, Rabitz H. Combust Sci Technol 1991;79(1–3):97–128.
[38] Kim TJ, Yetter RA, Dryer FL. Proc Combust Inst 1994;25: 759–66.
[39] Frenklach M, Bowman CT, Smith GP, Gardiner WC. World Wide Web location http://www.me.berkeley.edu.gri_mech/, Version 3.0, 1999.
[40] Yetter M, Shepherd JE. World Wide Web location http://www.galcit.caltech.edu/EDL/mechanisms/library/library.html
[41] Christiansen EW, Law CK, Sung CJ. Combust Flame 2001;124(1–2):35–49.
[42] Brown TM, Tanoff MA, Osborne RJ, Pitz RW, Smooke MD. Combust Sci Technol 1997;129:71–88.
[43] Sun CJ, Sung CJ, He L, Law CK. Combust Flame 1999; 118(1–2):108–28.
[44] Wu CK, Law CK. Proc Combust Inst 1984;20:1941–9.
[45] Aung KT, Hassan MI, Faeth GM. Combust Flame 1997; 109(1–2):1–24.